Total-Body PET Multiparametric Imaging of Cancer Using a Voxelwise Strategy of Compartmental Modeling

Guobao Wang[1], Lorenzo Nardo[1], Mamta Parikh[2], Yasser G. Abdelhafez[1], Elizabeth Li[3], Benjamin A. Spencer[1,3], Jinyi Qi[3], Terry Jones[1], Simon R. Cherry[1,3], and Ramsey D. Badawi[1,3]

[1]Department of Radiology, University of California Davis Medical Center, Sacramento, California; [2]UC Davis Comprehensive Cancer Center, Sacramento, California; and [3]Department of Biomedical Engineering, University of California at Davis, Davis, California

Quantitative dynamic PET with compartmental modeling has the potential to enable multiparametric imaging and more accurate quantification than static PET imaging. Conventional methods for parametric imaging commonly use a single kinetic model for all image voxels and neglect the heterogeneity of physiologic models, which can work well for single-organ parametric imaging but may significantly compromise total-body parametric imaging on a scanner with a long axial field of view. In this paper, we evaluate the necessity of voxelwise compartmental modeling strategies, including time delay correction (TDC) and model selection, for total-body multiparametric imaging. **Methods:** Ten subjects (5 patients with metastatic cancer and 5 healthy volunteers) were scanned on a total-body PET/CT system after injection of 370 MBq of ^{18}F-FDG. Dynamic data were acquired for 60 min. Total-body parametric imaging was performed using 2 approaches. One was the conventional method that uses a single irreversible 2-tissue-compartment model with and without TDC. The second approach selects the best kinetic model from 3 candidate models for individual voxels. The differences between the 2 approaches were evaluated for parametric imaging of microkinetic parameters and the ^{18}F-FDG net influx rate, K_i. **Results:** TDC had a nonnegligible effect on kinetic quantification of various organs and lesions. The effect was larger in lesions with a higher blood volume. Parametric imaging of K_i with the standard 2-tissue-compartment model introduced vascular-region artifacts, which were overcome by the voxelwise model selection strategy. **Conclusion:** The time delay and appropriate kinetic model vary in different organs and lesions. Modeling of the time delay of the blood input function and model selection improved total-body multiparametric imaging.

Key Words: image processing; PET; radiotracer tissue kinetics; compartmental modeling; parametric imaging; total-body dynamic PET

PET allows for dynamic scanning to monitor the spatiotemporal distribution of a radiotracer in the living body. With tracer kinetic modeling (e.g., compartmental models or graphical methods (1)), dynamic PET allows quantification of kinetic parameters in regions of interest (ROIs) and voxelwise (i.e., parametric imaging) (2,3). PET parametric imaging has the potential to improve tumor contrast, derive meaningful biologic measures of tracer

transport and binding, and enable quantitative assessment of tumor response to cancer treatment as compared with SUV (4). As the axial length of conventional PET scanners commonly ranges from 15 to 30 cm, clinical studies using dynamic PET have typically been limited to a restricted axial field of view that can cover only single organs or specific tumor locations. Whole-body implementation of parametric imaging has been pursued using conventional PET scanners but is limited mainly to the simplified Patlak graphical method (5–7), which is computationally efficient but does not explore the full potential of kinetic modeling for multiparametric imaging.

The advent of PET scanners with an extended long axial field of view, such as the uEXPLORER (United Imaging) (8–10), the PennPET Explorer (11,12), and the Quadra (Siemens) (13), is providing a paradigm shift in dynamic imaging. The longest of these has an axial field of view of 194 cm, providing not just unprecedented photon detection sensitivity but also simultaneous dynamic imaging and parametric imaging of the entire body (9,14). Image-derived input function (IDIF) can also be obtained from the left ventricle or the aorta. Metastatic lesions that are widely separated can now be imaged at the same time with total-body PET. The objective of this work was to conduct a pilot clinical study to test the feasibility of multiparametric imaging with compartmental modeling in total-body dynamic PET.

A typical approach to PET parametric imaging is to apply a single model to all voxels in the image (6,14,15). This approach can be appropriate for conventional single-organ parametric imaging but becomes insufficient for total-body parametric imaging in which organ- and tissue-appropriate models are required. In this work, we evaluated a voxelwise compartmental modeling strategy for total-body PET multiparametric imaging.

MATERIALS AND METHODS

Total-Body Dynamic PET/CT Image Acquisition

Ten subjects, including 5 patients with metastatic genitourinary cancer and 5 healthy volunteers, were recruited into this study at the University of California (UC) Davis Medical Center. Prior Ethics Committee and Institution Review Board approval and written informed consent were obtained. Patients were enrolled and scanned before the initialization of targeted therapy or immunotherapy. All subjects fasted for at least 6 h before the study.

PET/CT imaging was performed on the uEXPLORER total-body system at the UC Davis EXPLORER Molecular Imaging Center. Each subject had a total-body CT scan from head to toe with arms down, followed by a 60-min dynamic PET scan using an injection of approximately 370 MBq (10 mCi) of ^{18}F-FDG. List-mode data were acquired and binned into 29 frames: 6×10 s, 2×30 s, 6×60 s, 5×120 s, 4×180 s, and 6×300 s. Each frame was reconstructed into an image
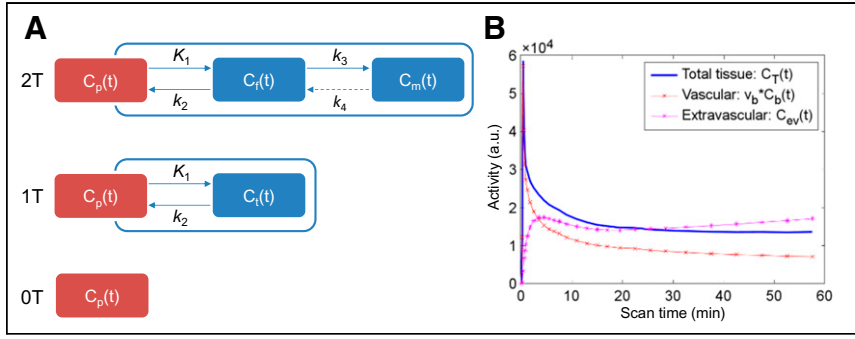
FIGURE 1. Compartmental modeling of ^{18}F-FDG. (A) 2T model and reduced 1T and 0T models. (B) Graph of time courses of ^{18}F-FDG in vascular and extravascular spaces that constitute total tissue time–activity curve. a.u. = arbitrary units.

of size $150 \times 50 \times 486$ with $4 \times 4 \times 4$ mm voxels using the vendor implementation of the time-of-flight ordered-subset expectation maximization algorithm with 4 iterations and 20 subsets. Standard corrections, including normalization, attenuation correction, dead-time correction, decay correction, random correction, and scatter correction, were all applied (*10*).

Compartmental Modeling and Parametric Imaging

Lesion Selection and ROI Placement. For each scan, ROIs were placed in various organs and on suspected lesions to extract regional time–activity curves. Up to 5 target lesions (maximum, 2 per organ) were identified per scan. The lesion ROIs were defined using 41% of the SUV$_{max}$ (at 60 min after injection) in each lesion (*16*). An additional ROI was placed in the ascending aorta using both early-frame and late-frame images as guidance to extract an IDIF, which is denoted by $C_{IDIF}(t)$. Lesion were delineated using AMIDE software (*17*).

Compartmental Models. The commonly used irreversible 2-tissue-compartment (2T) model (Fig. 1A) (*1*) was used to model the dynamic ^{18}F-FDG PET data. The corresponding ordinary differential equation of this 2T model is…

$$\frac{d}{dt}\begin{bmatrix} C_f(t) \\ C_m(t) \end{bmatrix} = \begin{bmatrix} -(k_2+k_3) & 0 \\ k_3 & 0 \end{bmatrix}\begin{bmatrix} C_f(t) \\ C_m(t) \end{bmatrix} + \begin{bmatrix} K_1 \\ 0 \end{bmatrix}C_p(t), \quad \text{(Eq. 1)}$$

where $C_p(t)$ is the ^{18}F-FDG concentration in the plasma, $C_f(t)$ is the concentration of free ^{18}F-FDG and $C_m(t)$ is the concentration of metabolized tracer in the tissue space at time t. The constant K_1 is the rate of ^{18}F-FDG delivery from the plasma to the tissue space in units of mL/min/cm^3 (*18*); k_2 (min^{-1}) is the rate constant of tracer exiting the tissue space; k_3 (min^{-1}) is the rate constant of ^{18}F-FDG being phosphorylated. This irreversible model assumes that the dephosphorylation process is negligible (i.e., $k_4=0$). The total concentration of ^{18}F-FDG in the extravascular space is…

$$C_{ev}(t) = C_f(t) + C_m(t) = H(t;\kappa) \otimes C_p(t), \quad \text{(Eq. 2)}$$

where $\kappa = [K_1, k_2, k_3]^T$ and $H(t;\kappa)$ is the impulse response function defined by…

$$H(t;\kappa) = \frac{K_1 k_3}{k_2+k_3} + \frac{K_1 k_2}{k_2+k_3}e^{-(k_2+k_3)t}. \quad \text{(Eq. 3)}$$

The macro parameters K_i (net influx rate) and V_0 (initial volume of distribution) can be calculated by (*5,19*)…

$$K_i = \frac{K_1 k_3}{k_2+k_3}, \quad V_0 = \frac{K_1 k_2}{(k_2+k_3)^2}. \quad \text{(Eq. 4)}$$

The total radioactivity that can be measured by PET is modeled as the sum of the time courses of ^{18}F-FDG in the vascular and

extravascular spaces (Fig. 1B):

$$C_T(t) = (1-v_b)C_{ev}(t) + v_b C_b(t), \quad \text{(Eq. 5)}$$

where v_b (mL/mL) is the fractional blood volume and $C_b(t)$ represents the whole blood.

Modeling of Voxelwise Time Delay in IDIF. A time delay exists between where the IDIF is extracted and the arrival of the radiotracer in the tissue of interest. Within the limited axial field of view of conventional PET scanners, the time delay effect has been commonly neglected because of the short distance between an IDIF and tissue ROIs, especially if the temporal resolution is low (e.g., 20–40 s per frame). Accounting for the time delay has conventionally been considered necessary only for fast kinetics when relatively high temporal sampling is used (*20,21*). A recent example was shown by Feng et al. (*22*) for fast total-body imaging of early ^{18}F-FDG kinetics. In our work, whereas the dynamic scan used a standard temporal resolution (10 s/frame), we noted the long distance between the ascending aorta and distant lesions, as well as potentially high vascular contributions in some lesions. Hence, the time delay effect is explicitly modeled in the blood input to each voxel by…

$$C_T(t) = (1-v_b)H(t;\kappa) \otimes C_p(t-t_d) + v_b C_b(t-t_d), \quad \text{(Eq. 6)}$$

with the time delay parameter t_d to be jointly estimated with other kinetic parameters though the time–activity curve fitting of a voxel. We postulate that time delay correction (TDC) has a higher impact on kinetic quantification if the fractional blood volume, v_b, is larger in the tissue, because the increased fraction of the vascular time course in turn influences the estimate of the extravascular time course, $C_{ev}(t)$, as projected from Figure 1B.

Fitting Optimization and Setting. A measured time–activity curve, $\check{C}_T(t)$, is fitted with the model time–activity curve, $C_T(t)$, using a nonlinear least-square formulation:

$$\hat{\theta} = \arg\min_\theta RSS(\theta), \quad RSS(\theta) = \sum_{m=1}^M w_m[\check{C}_T(t_m) - C_T(t_m)]^2, \quad \text{(Eq. 7)}$$

where $RSS(\theta)$ denotes the residual sum of squares of the curve fitting. θ is the unknown parameter set. For the irreversible 2T model, $\theta = [v_b, K_1, k_2, k_3, t_d]^T$. t_m is the midpoint of the mth frame in a total of M frames, and w_m is the weight for frame m. Given our interest in both K_i and K_1, a uniform weight was used as suggested by prior studies (*23–25*) (also demonstrated in Supplemental Fig. 1; supplemental materials are available at http://jnm.snmjournals.org).

The classic Levenberg–Marquardt algorithm with 50 iterations was used to solve the optimization problem in a similar way to our other work (*26*) and was implemented using C/C++ programming.

TABLE 1
Models Used for Dynamic ^{18}F-FDG PET Kinetic Modeling

Model order	Unknown parameters (n)	Kinetic parameters to be estimated
2T	5	v_b, K_1, k_2, k_3, t_d
1T	4	v_b, K_1, k_2, t_d
0T	2	v_b, t_d

TABLE 2
Subject Characteristics

Subject	Age (y)	Sex	BMI (kg/m^2)	Blood glucose level (mg/dL)	Fasting (h)	Disease	Initial therapy
1	78	M	24.4	101	11	Healthy	NA
2	26	M	33.8	77	6	Healthy	NA
3	50	M	27.2	94	12	Healthy	NA
4	51	F	24.2	93	12	Healthy	NA
5	62	M	29.5	92	12	Healthy	NA
6	65	M	32.0	154	12	CC RCC grade 2	Partial nephrectomy
7	62	M	26.3	84	8	CC RCC grade 4	Radical nephrectomy
8	65	M	25.3	65	20	CC RCC grade 3	Radical nephrectomy
9	76	M	20.1	128	10	CC RCC grade 2	Radical nephrectomy
10	70	M	24.3	131	11	High-grade TCC	Radical cystectomy

BMI = body mass index; NA = not applicable; CC RCC = clear cell renal cell carcinoma; TCC = transitional cell carcinoma.
All cancer patients had stage IV disease. Fuhrman grade was used.

The initial values of κ and v_b were set to $[0.01, 0.01, 0.01]^T$ and 0.01, respectively. The lower bound was zero and the upper bound was $[5.0, 5.0, 1.0]^T$ and 1.0, respectively. The time delay, t_d, was jointly estimated by a grid search with the lower and upper bounds set to -10 and 50 s, respectively.

Voxelwise Model Selection. Conventionally for simplicity, parametric imaging uses a single kinetic model (e.g., the irreversible 2T model) for all voxels. In total-body parametric imaging, a wide physiologic heterogeneity may exist within the field of view. In addition to the 2T model, we also considered the 1-tissue-compartment (1T) model and zero-tissue-compartment (0T) model (Fig. 1A; Table 1). The 0T model is more suitable for those voxels containing only blood. The 1T model is equivalent to the 2T model with $k_3 = 0$, implying that the phosphorylation process can be neglected when k_3 is small and the data are noisy. The 0T model is a special case of the 1T model with $K_1 = 0$. The best model was chosen for each voxel j from a set of candidate models (0T, 1T, and 2T in Table 1) according to the minimum Akaike information criterion (AIC),

$$l_j = \text{argmin}_l \ \text{AIC}_j(l), \quad (\text{Eq. 8})$$

where $\text{AIC}_j(l)$ denotes the AIC of model order l ($l = 0, 1, 2$) for fitting the time–activity curve at voxel j. The AIC with correction for a small number of frames is calculated by (27)...

$$\text{AIC} = M \ln(RSS/M) + 2n \quad (\text{Eq. 9})$$
$$+ 2n(n+1)/(M-n-1),$$

where RSS is calculated using Equation 7 for a specific model and n denotes the total number of unknown parameters in the model. A lower AIC value indicates a better model (27).

Parametric Imaging with Kernel Smoothing. Voxelwise implementation of compartmental modeling leads to the generation of parametric images of tracer kinetics, which usually suffer from high noise in voxels. The kernel method (28) was applied here as postreconstruction smoothing to reduce noise in the dynamic images, a process that is also equivalent to nonlocal means smoothing (28). Fundamentally, it rests on deriving, for each patient dataset, a kernel matrix built from 4 consecutive composite frames of 5, 15, 20, and 20 min, respectively. For each voxel, k-nearest neighbors with k
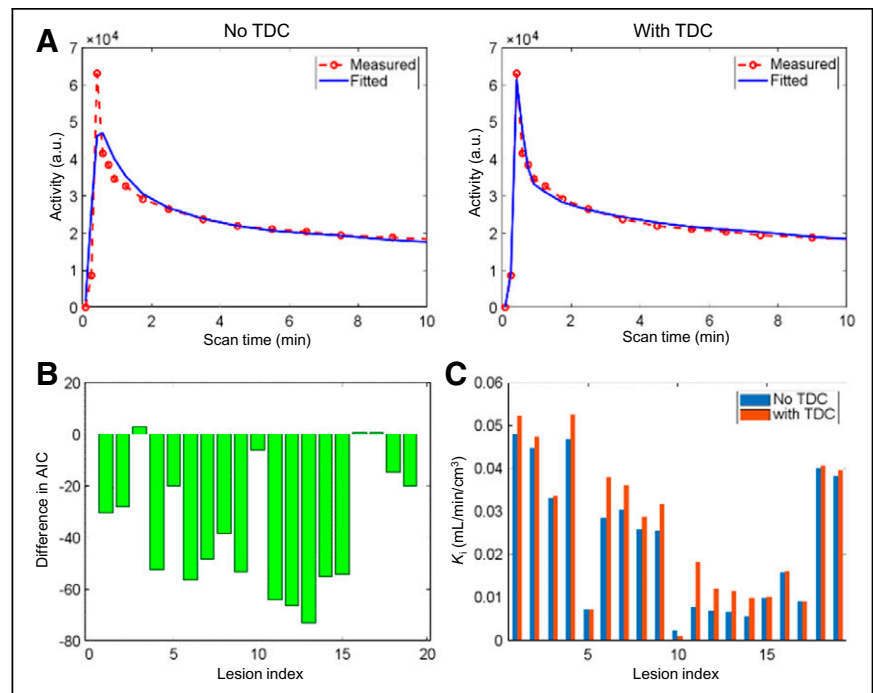
FIGURE 2. Graphs of time delay and its impact on lesion time–activity curve fitting and kinetic quantification. (A) Fitting of liver lesion time–activity curve with no TDC and with time delay jointly estimated. (B) AIC difference between 2T models with and without TDC for time–activity curve fitting in 19 lesions. (C) Comparison of K_i values for individual lesions. a.u. = arbitrary units.

TABLE 3
Mean and SD of Lesion Kinetic Parameters Estimated by 2T Model With and Without TDC

Parameter	Without TDC	With TDC	P of paired t test	P of paired signed-rank test
t_d (s)	0	7 ± 5	0.0001	0.0008
v_b (mL/cm^3)	0.027 ± 0.053	0.232 ± 0.181	0.0002	0.0002
K_1 (mL/min/cm^3)	0.974 ± 0.814	0.331 ± 0.383	0.0017	0.0002
K_i (mL/min/cm^3)	0.023 ± 0.016	0.026 ± 0.017	0.0003	0.0005
V_0 (mL/cm^3)	0.420 ± 0.267	0.380 ± 0.221	0.0161	0.0123

Paired t test and Wilcoxon signed-rank test were both used for calculating P value.

(number of nearest neighbors) = 50 was constructed in a cubic 9 × 9 × 9 voxel space. More details of the method have been previously published (28). The same kernel matrix was also applied to the parametric images for further noise suppression.

Statistical Analysis

Statistical data were analyzed mainly for demonstrating the impact of TDC and model selection. To evaluate the effect of TDC, linear regression analysis and a group comparison were performed for different kinetic parameters of lesions using the paired Student t test and Wilcoxon signed-rank test. A P value of less than 0.05 was considered statistically significant. For assessing the impact of model selection, artifacts in the K_i parametric images were identified visually in blood regions. AIC was calculated to indicate a potential overfitting of the blood time–activity curves.

RESULTS

#### Patient Characteristics and Image Data

Table 2 lists the characteristics of the study subjects. All dynamic scans of the 5 healthy subjects and 5 cancer patients were successful. Nineteen lesions were identified on the SUV images of the cancer patients. Supplemental Figure 2 shows the dynamic ^{18}F-FDG PET images and regional time–activity curves for 2 patients with cancer. The 2 patients shared a similar time–activity curve shape for the brain and liver, but the time–activity curves of the lesions were very different.

Effect of Time Delay Correction (TDC)

Figure 2 shows the results of applying TDC by joint estimation to fit lesion time–activity curves using the 2T model. The TDC resulted in an improvement in fitting the lesion time–activity curve, particularly in the early phase where the peak is. The improved fit is further evidenced by a statistical quality evaluation using AIC in the lesions (Fig. 2B). A lower AIC was achieved by the TDC in most lesions. The individual lesion K_i values by the 2 approaches are

shown in Figure 2C. Generally, K_i became higher after TDC. The percentage change in K_i and K_1 was further plotted against the fractional blood volume v_b in Supplemental Figure 3. As v_b increased, the difference in the 2 approaches became larger for both K_i and K_1.

Table 3 summarizes the kinetic results estimated by the 2 approaches (i.e., with and without TDC) in all lesions. The time delay was 7 ± 5 s (range, −2 to 18 s), which is significantly different from zero as indicated by the small P value of the statistical tests.
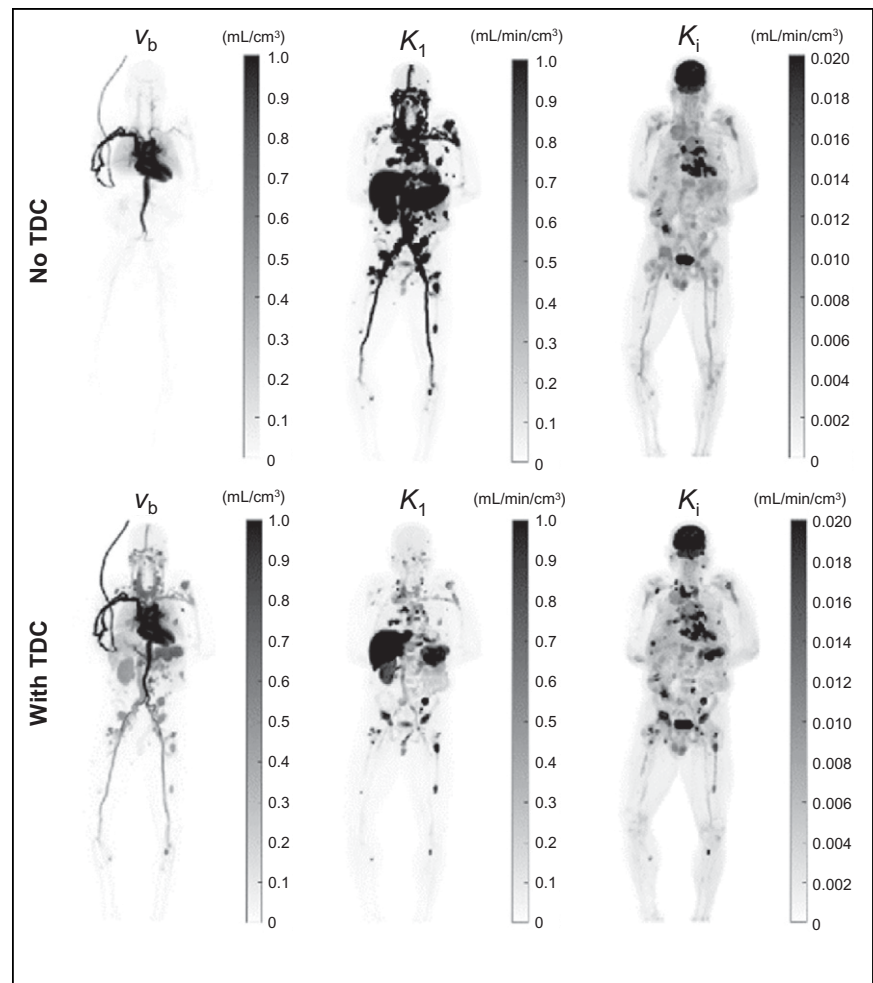
FIGURE 3. Demonstration of parametric imaging using 2T model with and without TDC for cancer patient. Shown are maximum-intensity-projection maps for v_b, K_1, and K_i.
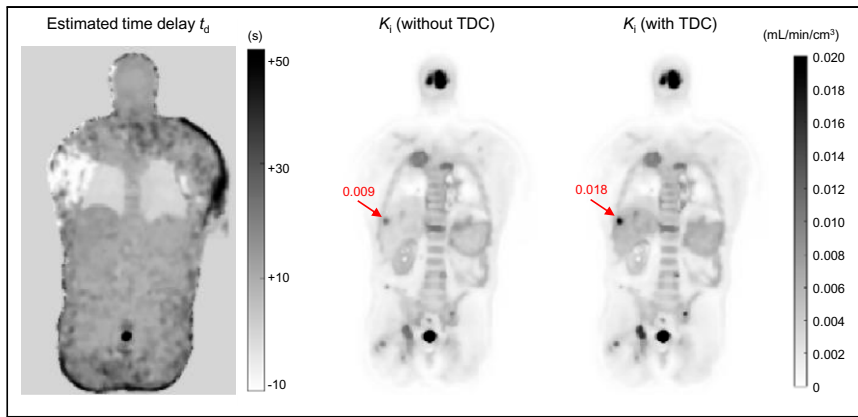
FIGURE 4. Coronal plane of estimated time delay t_d map and K_i parametric images with and without TDC for cancer patient. Arrows point to liver lesion.

TDC led to a much higher v_b and appreciably lower K_1 estimates ($P < 0.002$). Although the mean and SD of K_i in the pooled analysis had only a small difference between the 2 approaches, the paired statistical tests show TDC had a statistically significant effect ($P \leq 0.0005$) on K_i estimation, as reflected by the pairwise changes shown in Figure 2C and Supplemental Figure 3. The impact on V_0 was also statistically significant ($P < 0.02$).

Examples of parametric images of different kinetic parameters are shown in Fig. 3 for 1 cancer patient. Without TDC, the v_b image did not show all the vasculature, especially in the legs, where the time delay was large. The K_1 image became clearer after the TDC because the vasculature disappeared in this image. Fig. 4 further shows the estimated time delay map and K_i images. Lesions were less visible with low K_i values if no TDC was implemented; most lesions were enhanced, with a higher value after TDC.

Effect of Voxelwise Model Selection

Figure 5A shows the map of the model order (0T, 1T, and 2T) selected for individual voxels for a cancer patient scan. Most body parts, such as soft tissues, followed the 2T model, whereas the lungs and skin favored the 1T model according to AIC. Vascular regions (e.g., the heart chambers and arteries) followed the 0T model. All lesions followed the 2T model. The parametric image of K_i generated using a single 2T model (Fig. 5B) contains a suggestive hot spot of a high K_i value. It disappeared after applying voxelwise model selection. Figure 5C demonstrates that both the 2T and the 0T models fitted the time–activity curve well but that the resulting K_i values were very different (0.018 vs. 0.0 mL/min/cm³). The AICs of different fits by the 0T, 1T, and 2T models are compared in Figure 5D. It indicates that the 0T model was best for fitting the blood time–activity curve, whereas the 2T model overfitted the time–activity curve and resulted in a falsely high value of K_i.

Figure 6 compares the conventional single 2T model (with TDC) with the proposed method (with model selection and TDC) for parametric imaging of K_i at the

level of the heart in all 10 subjects. The conventional method resulted in artificially high K_i values in some voxels containing primarily blood. The myocardium was also difficult to visualize in each patient scan. In comparison, the proposed method largely removed those artifacts, and appropriate model selection led to clear visualization of the myocardium in all subjects.

Demonstration of Multiparametric Images

With the improved voxelwise modeling strategy, we show parametric images for a range of kinetic parameters, including v_b, K_1, K_i, and V_0, for 1 cancer patient in Figure 7 and for 1 healthy subject in Supplemental Figure 4. The SUV images at 60 min after injection are also included. Although the K_i and SUV images share similar information in most patients, the v_b, K_1, and V_0 images demonstrate very different spatial patterns in the body, thus providing information complementary to that provided by SUV. Supplemental Figure 5 demonstrates that parametric images can potentially be more useful than SUV for liver tumor imaging and brain tumor imaging.

DISCUSSION

In this paper, we have evaluated a voxelwise strategy for total-body ^{18}F-FDG PET parametric imaging using compartmental modeling. TDC through joint estimation during time–activity curve fitting was found to be significant (Fig. 2) and had a high impact on quantification and parametric imaging of v_b and K_1 (Table 3; Fig. 3). The impact on K_i was of lesser extent when v_b was small but became higher as v_b increased (Fig. 4; Supplemental Figure 3). Dispersion correction was not explicitly included in this study, but the incorporation of v_b may partly account for the
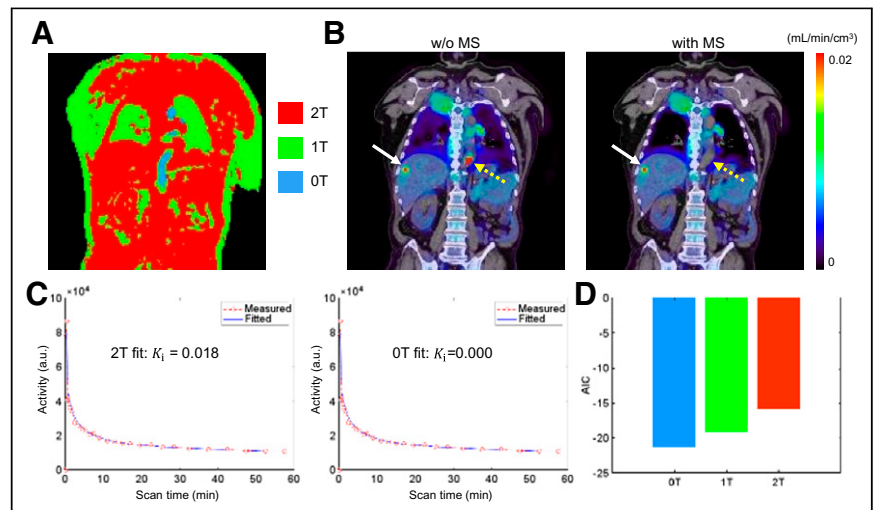
FIGURE 5. Evaluation of impact of model selection (MS). (A) Distribution map of different kinetic models (0T, 1T, and 2T). (B) Parametric image of K_i (overlaid on CT images) by 2T model with and without (w/o) voxelwise MS. Solid arrows point to potential lesions, and dashed arrows point to blood voxels in descending aorta. (C) Blood time–activity curve fitted with 2T and 0T models. (D) AIC values of 3 models (0T, 1T, and 2T). a.u. = arbitrary units.
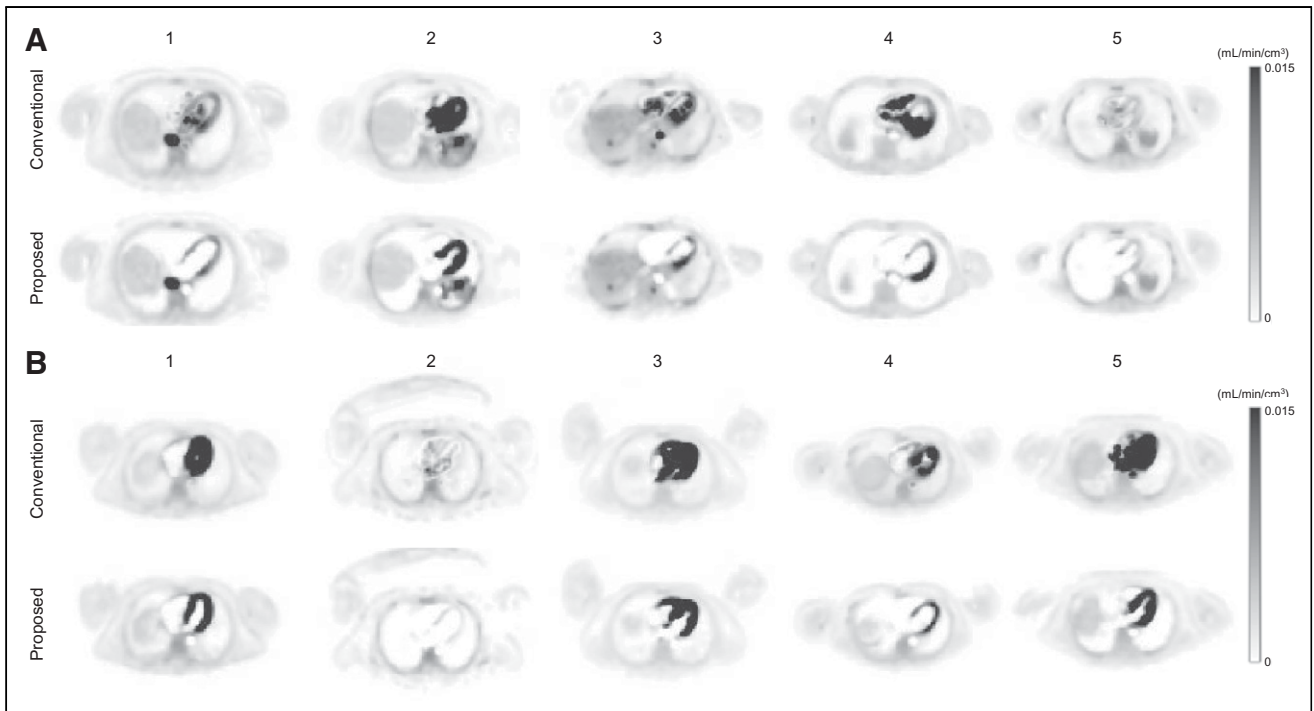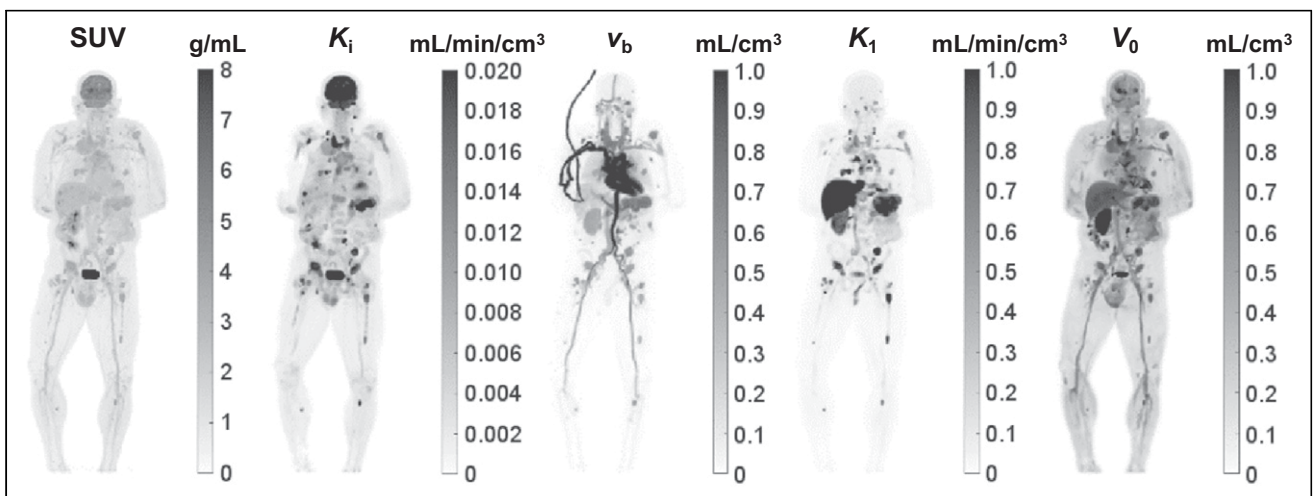
FIGURE 6. Comparison of ^{18}F-FDG K_i parametric images generated by conventional 2T model (with TDC) and proposed approach that includes model selection and TDC in 5 patients with cancer (A) and 5 healthy subjects (B).

potential dispersion effect (*29*). The v_b values of lesions estimated in this study were relatively high (0.23 ± 0.18 mL/cm³), as likely reflects that most patients had clear cell renal cell carcinoma, which tends to be highly vascular (*30*). It is also perhaps because v_b is more like a method parameter than being quantitative, given that it also accounts for the dispersion effect.

Our study also found that the standard 2T model led to artificially high values in the K_i image in those voxels containing primarily blood. This effect was caused by overfitting of the time–activity curves that better follow the 0T model or 1T model, as indicated by the AIC comparison (Fig. 5). We addressed this problem by applying voxelwise model selection using AIC. The method led to clear

visualization of the myocardium, whereas the standard model did not (Fig. 6). The AIC-based model selection is driven by a statistical fit quality evaluation and cannot be overinterpreted physiologically. For example, the choice of 1T over 2T does not indicate the nonexistence of phosphorylation but suggests that k_3 can be neglected when the data are noisy. As an alternative to AIC, other approaches are also possible by applying sparsity constraints to kinetic parameters or using sparse spectral analysis (*31*). In addition, factor analysis (*32*) and mixture models (*33*) could also be advantageous to explore in total-body parametric imaging (*34*).

As the first step for demonstrating a workable modeling strategy, we considered only the irreversible 2T model. This model is

FIGURE 7. Comparison of standard SUV image with parametric images of ^{18}F-FDG influx rate K_i, fractional blood volume v_b, ^{18}F-FDG delivery rate K_1, and volume of distribution V_0 images of cancer patient. Shown are maximum-intensity-projection maps.

appropriate when the dephosphorylation process is negligible during the 1-h dynamic scan time. However, the reversible 2T model (with $k_4 > 0$) can be more appropriate for kinetic quantification of organs such as the liver (*35*) and myocardium (*36*). The liver and lungs also receive dual blood supplies and require modeling of their dual-blood input function for accurate kinetic quantification. These aspects were not addressed in this study. Motion correction may also further improve the quantification performance. Implementation of these more complex models in total-body parametric imaging is a part of our ongoing effort.

The focus of this paper was mainly on the methodologic implementation for multiparametric imaging using compartmental modeling. Because of the page limit, the benefits of parametric images have not been directly compared with the SUV images (other than Supplemental Fig. 5) and with the parametric images determined from the linear Patlak plot (*5,14,37*). In general, multiparametric imaging with compartmental modeling not only generates K_i and V_0 but can also provide other microkinetic parameters, including v_b and K_1 (Fig. 7), that go beyond what the Patlak method can offer. Exploring the potential benefits of these multiparametric images will be reported in future work.

This study had several other limitations. The temporal sampling rate for early dynamic scanning was relatively limited (10 s/frame) but was a reasonable choice based on our preliminary study as shown in Supplemental Figure 6. Within this context, the time delay t_d is mainly a method parameter that is coarsely estimated. Optimal sampling (trade-off between temporal resolution and voxel noise level) and the effect on kinetic quantification remain to be further investigated. In addition, the number of studied subjects was relatively small, and the study did not have a reference or outcome measure to evaluate the impact of kinetic quantification. The studied cancer type was also limited to genitourinary cancer. It will be worth evaluating the proposed kinetic modeling strategies in other cancers. Future studies will take these aspects into account.

CONCLUSION

We successfully conducted total-body PET multiparametric imaging using compartmental modeling for the dynamic ^{18}F-FDG PET data acquired on the uEXPLORER system in both healthy subjects and cancer patients. TDC led to improved lesion time–activity curve fitting, physiologically more consistent vasculature in the v_b image, and a generally higher K_i in lesions, especially when v_b was large. Voxelwise model selection reduced artifacts in the K_i parametric images and led to clearer visualization of the myocardium. Both the modeling of time delay of the blood input function and model selection are necessary for accurate total-body multiparametric imaging.

DISCLOSURE

KEY POINTS

QUESTION: Is it feasible to perform multiparametric imaging with compartmental modeling in total-body dynamic PET of cancer?

PERTINENT FINDINGS: Voxelwise modeling of the time delay of the blood input function and model selection are necessary for accurate total-body multiparametric imaging.

IMPLICATIONS FOR PATIENT CARE: Total-body dynamic PET can enable single-tracer multiparametric imaging, which may be further explored to improve tumor detection and treatment response assessment.

REFERENCES

1. Morris ED, Endres CJ, Schmidt KC, Christian BT, Muzic RF, Fisher RE. Kinetic modeling in positron emission tomography. In: Wermick MN, JN A, eds. *Emission Tomography: The Fundamentals of PET and SPECT*. Elsevier Inc.; 2004:499–540.
2. Gallezot JD, Lu YH, Naganawa M, Carson RE. Parametric imaging with PET and SPECT. *IEEE Trans Radiat Plasma Med Sci.* 2020;4:1–23.
3. Wang G, Rahmim A, Gunn RN. PET parametric imaging: past, present, and future. *IEEE Trans Radiat Plasma Med Sci.* 2020;4:663–675.
4. Dimitrakopoulou-Strauss A, Pan LY, Sachpekidis C. Kinetic modeling and parametric imaging with dynamic PET for oncological applications: general considerations, current clinical applications, and future perspectives. *Eur J Nucl Med Mol Imaging.* 2021;48:21–39.
5. Rahmim A, Lodge MA, Karakatsanis NA, et al. Dynamic whole-body PET imaging: principles, potentials and applications. *Eur J Nucl Med Mol Imaging.* 2019;46:501–518.
6. Karakatsanis NA, Lodge MA, Tahari AK, Zhou Y, Wahl RL, Rahmim A. Dynamic whole body PET parametric imaging: I. Concept, acquisition protocol optimization and clinical application. *Phys Med Biol.* 2013;58:7391–7418.
7. Hu JC, Panin V, Smith AM, et al. Design and implementation of automated clinical whole body parametric PET with continuous bed motion. *IEEE Trans Radiat Plasma Med Sci.* 2020;4:696–707.
8. Cherry SR, Jones T, Karp JS, Qi J, Moses WW, Badawi RD. Total-body PET: maximizing sensitivity to create new opportunities for clinical research and patient care. *J Nucl Med.* 2018;59:3–12.
9. Badawi RD, Shi H, Hu P, et al. First human imaging studies with the EXPLORER total-body PET scanner. *J Nucl Med.* 2019;60:299–303.
10. Spencer BA, Berg E, Schmall JP, et al. Performance evaluation of the uEXPLORER total-body PET/CT scanner based on NEMA NU 2-2018 with additional tests to characterize PET Scanners with a long axial field of view. *J Nucl Med.* 2021;62:861–870.
11. Pantel AR, Viswanath V, Daube-Witherspoon ME, et al. PennPET Explorer: human imaging on a whole-body imager. *J Nucl Med.* 2020;61:144–151.
12. Karp JS, Schmall J, Geagan M, et al. Imaging performance of the PennPET Explorer scanner [abstract]. *J Nucl Med.* 2018(suppl 1);59:222.
13. Alberts I, Hunermund JN, Prenosil G, et al. Clinical performance of long axial field of view PET/CT: a head-to-head intra-individual comparison of the Biograph Vision Quadra with the Biograph Vision PET/CT. *Eur J Nucl Med Mol Imaging.* 2021;48:2395–2404.
14. Zhang X, Xie ZH, Berg E, et al. Total-body dynamic reconstruction and parametric imaging on the uEXPLORER. *J Nucl Med.* 2020;61:285–291.
15. Gunn RN, Lammertsma AA, Hume SP, Cunningham VJ. Parametric imaging of ligand-receptor binding in PET using a simplified reference region model. *Neuroimage.* 1997;6:279–287.
16. Boellaard R, Delgado-Bolton R, Oyen WJG, et al. FDG PET/CT: EANM procedure guidelines for tumour imaging—version 2.0. *Eur J Nucl Med Mol Imaging.* 2015;42:328–354.
17. Loening AM, Gambhir SS. AMIDE: a free software tool for multimodality medical image analysis. *Mol Imaging.* 2003;2:131–137.

18. Innis RB, Cunningham VJ, Delforge J, et al. Consensus nomenclature for in vivo imaging of reversibly binding radioligands. *J Cereb Blood Flow Metab.* 2007;27: 1533–1539.

19. Gunn RN, Gunn SR, Cunningham VJ. Positron emission tomography compartmental models. *J Cereb Blood Flow Metab.* 2001;21:635–652.

20. Iida H, Higano S, Tomura N, et al. Evaluation of regional difference of tracer appearance time in cerebral tissues using O-15 water and dynamic positron emission tomography. *J Cereb Blood Flow Metab.* 1988;8:285–288.

21. Lammertsma AA, Cunningham VJ, Deiber MP, et al. Combination of dynamic and integral methods for generating reproducible functional CBF images. *J Cereb Blood Flow Metab.* 1990;10:675–686.

22. Feng T, Zhao Y, Shi H, Li H, et al. Total-body quantitative parametric imaging of early kinetics of ^{18}F-FDG. *J Nucl Med.* 2021;62:738–744.

23. Thiele F, Buchert R. Evaluation of non-uniform weighting in non-linear regression for pharmacokinetic neuroreceptor modelling. *Nucl Med Commun.* 2008; 29:179–188.

24. Winterdahl M, Munk OL, Sorensen M, Mortensen FV, Keiding S. Hepatic blood perfusion measured by 3-minute dynamic F-18-FDG PET in pigs. *J Nucl Med.* 2011;52:1119–1124.

25. Yaqub M, Boellaard R, Kropholler MA, Lammertsma AA. Optimization algorithms and weighting factors for analysis of dynamic PET studies. *Phys Med Biol.* 2006;51:4217–4232.

26. Wang G, Qi J. An optimization transfer algorithm for nonlinear parametric image reconstruction from dynamic PET data. *IEEE Trans Med Imaging.* 2012; 31:1977–1988.

27. Burnham KP, Anderson DR. Multimodel inference: understanding AIC and BIC in model selection. *Sociol Methods Res.* 2004;33:261–304.

28. Wang G, Qi J. PET image reconstruction using kernel method. *IEEE Trans Med Imaging.* 2015;34:61–71.

29. Mourik JEM, van Velden FHP, Lubberink M, et al. Image derived input functions for dynamic High Resolution Research Tomograph PET brain studies. *Neuroimage.* 2008;43:676–686.

30. Chen Y, Zhang J, Dai JR, Feng XL, Lu HZ, Zhou CW. Angiogenesis of renal cell carcinoma: perfusion CT findings. *Abdom Imaging.* 2010;35:622–628.

31. Gunn RN, Gunn SR, Turkheimer FE, Aston JAD, Cunningham TJ. Positron emission tomography compartmental models: a basis pursuit strategy for kinetic modeling. *J Cereb Blood Flow Metab.* 2002;22:1425–1439.

32. Wu HM, Hoh CK, Buxton DB, et al. Quantification of myocardial blood flow using dynamic nitrogen-13-ammonia PET studies and factor analysis of dynamic structures. *J Nucl Med.* 1995;36:2087–2093.

33. O'Sullivan F. Imaging radiotracer model parameters in PET: a mixture analysis approach. *IEEE Trans Med Imaging.* 1993;12:399–412.

34. Viswanath V, Chitalia R, Pantel AR, Karp JS, Mankoff DA. Analysis of four-dimensional data for total body PET imaging. *PET Clin.* 2021;16:55–64.

35. Wang G, Corwin MT, Olson KA, Badawi RD, Sarkar S. Dynamic PET of human liver inflammation: impact of kinetic modeling with optimization-derived dual-blood input function. *Phys Med Biol.* 2018;63:155004.

36. Zuo Y, Badawi RD, Foster CC, Smith T, Lopez JE, Wang G. Multiparametric cardiac ^{18}F-FDG PET in humans: kinetic model selection and identifiability analysis. *IEEE Trans Radiat Plasma Med Sci.* 2020;4:759–767.

37. Dias AH, Pedersen MF, Danielsen H, Munk OL, Gormsen LC. Clinical feasibility and impact of fully automated multiparametric PET imaging using direct Patlak reconstruction: evaluation of 103 dynamic whole-body ^{18}F-FDG PET/CT scans. *Eur J Nucl Med Mol Imaging.* 2021;48:837–850.